High Redshift AGN: Accretion Rates and Morphologies for X-ray and Radio SC4K Sources from z∼2 to z∼6[⋆]

Benjamin Adams[1], Cameron Bishop[1], Matthew Fahey[1], Jordan Greener[1],
Jiayi Kong[1] & David Sobral[1]†

[1] *Department of Physics, Lancaster University, Lancaster, LA1 4YB, UK*

ABSTRACT

We study a large sample of ∼4000 Lyα Emitters (LAEs) and identify the active galactic nuclei (AGN) among them in order to characterise their evolution across cosmic time. This work was carried out using the SC4K survey (Sobral et al. 2018a) and data collected by the *Hubble Space Telescope (HST)*, *Chandra* X-ray Observatory and the Very Large Array (VLA). We find 322 X-ray or radio detected AGN within the sample, constituting 8.7±0.5% of the sources considered. We find the vast majority of classifiable AGN (81±3%) are point-like or compact sources in the rest-frame UV seen with *HST*, and this qualitative trend holds regardless of detection band or redshift. These AGN have a range of black hole accretion rates (BHARs), and we present the first direct comparison between radio and X-ray BHARs. X-ray calculated BHARs range from ∼ 0.07 M$_\odot$ yr^{-1} to ∼ 23 M$_\odot$ yr^{-1}, indicating a highly varied sample, with some very active AGN detected. Radio calculated BHARs range from ∼ 0.09 M$_\odot$ yr^{-1} to ∼ 8.8 M$_\odot$ yr^{-1}, broadly tracing the same range as the X-ray calculated BHARs. X-ray calculated BHARs peak at $z \sim 3$ and both radio and X-ray calculated BHARs increase with increasing redshift, plateauing at $z \sim 4$. We find significantly less variation in radio BHARs when compared to X-ray BHARs, indicating radio may be a far more stable and reliable method of calculating the BHARs of AGN over large timescales, while X-ray is more suitable for instantaneous BHARs.

Key words: accretion - galaxies: active - galaxies: evolution - galaxies: high-redshift - X-rays: galaxies: supermassive black holes.

1 INTRODUCTION

According to the standard cold dark matter (ΛCDM) cosmological model, galaxies initially formed several billion years ago from perturbations in the density of dark matter in the early Universe. These perturbations undergo gravitational clustering, progressively forming larger systems known as dark matter halos (White & Rees 1978). Gas condenses into the gravitational potential wells created by this dark matter, forming stars once sufficient gas has collapsed into the centre of the halo that it becomes self-gravitating, forming a giant molecular cloud complex which becomes dense enough to ignite nuclear fusion. Eventually a galaxy is formed, surrounded by its dark matter halo (Springel et al. 2005). As the

galaxies evolve, some stars within will eventually go supernova, which pollutes the intergalactic medium with heavy elements (Arnaud et al. 1992), helping initiate star and galaxy formation by enhancing cooling rates in gas clouds (see Somerville & Davé 2015, and references therein).

Supermassive black holes (SMBH) have been found to be at the centre of most galaxies (e.g. Kormendy & Richstone 1995; Green 2002; Ferrarese & Ford 2005), and have been found to have formed as early as 1 Gyr after the Big Bang, with masses up to 10^9 M$_\odot$ (e.g. Barth et al. 2003; Willott et al. 2005). Due to the early formation of these SMBH, they cannot have formed through conventional methods of black hole formation because of the Eddington accretion limit, and instead may have come from seed massive black holes (Davies et al. 2011). However, the exact formation process of these seeds is still unknown, and there are several possibilities as to how they could form (Volonteri 2010). These possibilities include: the remnants of PopIII stars (hypothetical stars containing virtually no

metals, see Madau & Rees 2001; Volonteri et al. 2003); being triggered by gas-dynamical instabilities (Lodato & Natarajan 2006; Begelman et al. 2006); and being formed by stellar-dynamical processes (Gürkan et al. 2006; Devecchi & Volonteri 2009).

Lyα emitters (LAEs) are galaxies that emit the hydrogen emission line Lyα (rest-frame 1216 Å), caused by the recombination of interstellar hydrogen that has been ionized by radiation (Malhotra & Rhoads 2002). Lyα is known to be strongly produced by both active galactic nuclei (AGN) activity and star formation (Charlot & Fall 1993; Hashimoto et al. 2017). The brightest LAEs are typically found to be AGN, with virtually all LAEs with a luminosity in excess of $10^{43.3}$ erg s^{-1} studied in Sobral et al. (2018b) being AGN. Additionally, the Lyα luminosities are found to correlate with the black hole accretion rates (BHAR) within the AGN (Calhau et al. 2020). From this it can be inferred that the source of the observed Lyα emissions is the black hole itself. The strength of the emission line produced is dependent on the relative gas and dust distributions in the circumgalactic and interstellar medium (Neufeld 1991; Laursen et al. 2013), as the photons generated by the LAEs are scattered by the gas and absorbed by the dust surrounding galaxies (Wisotzki et al. 2016). As a consequence of this, the LAEs observed tend to be younger and bluer galaxies with a low dust content, although studies have found more varied galaxies are able to be probed at this wavelength, including older, more red galaxies with a higher dust content (Oteo et al. 2015; Hathi & Le Fèvre 2016; Sobral et al. 2018a).

AGN are compact regions at the centre of some galaxies that have a much higher than normal luminosity. Current theory suggests that there is a SMBH at the centre of every AGN, surrounded by an accretion disk of gas (Netzer 2015). Feedback associated with these AGN can have an impact on galactic evolution, primarily through radiative transfer, and is an area of active research. For example, the AGN can heat gas directly through Compton scattering, photoionization, and photoelectric heating, known as thermal feedback (Rafferty et al. 2007; McNamara & Nulsen 2007). The AGN can also cause winds driven by radiation that eject gas from the galaxy, with the potential to create large-scale winds that can drive out interstellar gas (kinetic feedback; see Saez et al. 2009; Moe et al. 2009; Dunn et al. 2010).They may also ionize or photodissociate gas (radiative feedback; see Chen 2019). All of these processes can impact galactic evolution, primarily by hindering star formation and cooling within the entire galaxy, as well as regulating the growth of the black hole itself (Fabian 2012).

Thermal spectrum photons, produced by the frictional heating within the accretion disk can undergo inverse Compton scattering, colliding with ultrarelativistic electrons to obtain significantly higher energies (e.g. Shapiro et al. 1976; Pozdnyakov et al. 1983; Kubota et al. 2001). Inverse Compton scattering within the accretion disk results in the production of X-ray luminosities far in excess of those expected within typical galaxies from star formation (e.g. Sargsyan & Weedman 2009). Hence, X-ray luminosity serves as a key signature of AGN activity, and a cut-off luminosity of 10^{42} erg s^{-1} is typically used to distinguish between AGN and non-AGN sources (e.g. Barlow-Hall et al. 2019; Calhau et al. 2020). Furthermore, the nature of this X-ray production

means that X-ray luminosity directly traces the BHAR of the central SMBH.

The structure of AGN naturally lead to comparisons with black hole X-ray binary (BHXRB) systems, which also have a central engine comprising a black hole surrounded by an accretion disk (Körding et al. 2006). Previous studies have explored the BHARs of BHXRBs in a number of different accretion states, and have used the similarities with AGN to extrapolate radio BHAR relations to these far larger and more energetic sources (Körding et al. 2006, 2008). As such, this provides two independent methods of estimating the accretion rates for AGN sources, one using X-ray wavelengths and one using radio wavelengths.

Previous papers suggest that radio emission traces much longer timescales than X-ray, on the order of ∼100 million years (Calhau et al. 2017), and hence BHARs calculated using radio data could provide insight into the accretion rates of AGN in the past.

Furthermore, we know that the accretion rates of AGN can vary over time (e.g. Angione 1973; Marshall et al. 1981; Neugebauer et al. 1989) and that this variability is found in many wavelengths, with the timescale of the variation increasing with increasing wavelength. Hence, if this trend continues into the radio spectrum, radio data may be less susceptible to rapid change during these periods, giving us better insight into the overall nature of the accretion rate over long time periods. As such, a comparison between X-ray and radio accretion rates could be indicative of how AGN accretion varies over cosmic time.

In this paper we aim to explore the nature of the AGN sources in the SC4K sample across cosmic time. We investigate the accretion rates of these sources in relation to redshift and morphology to see if specific redshifts and morphologies are characterised by accretion rate trends. Furthermore, by studying the morphology of the sources we attempt to characterise the evolution of AGN across cosmic time. In addition, we test the accuracy of the Körding et al. (2006) relation for Radio BHAR by comparison with the well established X-ray BHAR and consider the implications of the radio BHAR for indicating AGN accretion in the past.

Our paper is organised in the following way. In Section 2 we present the SC4K catalogue utilised in this work. The methods used to identify the AGN, classify their morphologies and investigate their activity are presented in Section 3. Our results and discussion are presented in Section 4 and Section 5. Finally, the conclusions are presented in Section 6. Throughout this paper we use AB magnitudes (Oke & Gunn 1983), and we adopt the following flat cosmology: $H_0 = 70.0$ kms^{-1}Mpc^{-1}, $\Omega_M = 0.3$ and $\Omega_\Lambda = 0.7$.

2 SAMPLE

2.1 SC4K: Lyα emitters at $z \sim 2 - 6$

The SC4K sample consists of ∼4000 LAEs in the COSMOS field across 16 different redshift slices ranging from redshift $z \sim 2 - 6$. The redshift slices are imaged in 12 medium and 4 narrow band filters by the Subaru Telescope and the Isaac Newton Telescope respectively, as detailed in Sobral et al. (2018a).

LAEs are selected by examining the emission line equivalent width (EW), the strength of the Lyα emission line,

for each detected source. This is calculated in Sobral et al. (2018a) as:

$$\mathrm{EW_{obs}} = \Delta\lambda_{\mathrm{MB}} \frac{f_{\mathrm{MB}} - f_{\mathrm{BB}}}{f_{\mathrm{BB}} - f_{\mathrm{MB}}(\Delta\lambda_{\mathrm{MB}}/\Delta\lambda_{\mathrm{BB}})} \qquad (1)$$

Where f_{MB} and f_{BB} are the flux densities of the medium band (MB) and broad band (BB) filters respectively, and $\Delta\lambda_{\mathrm{MB}}$ and $\Delta\lambda_{\mathrm{BB}}$ are the full width at half maximum (FWHM) of these two filters.

Sources that had $\mathrm{EW} > 50(1+z)$ Å or $\mathrm{EW}_0 > 50$ Å (where $\mathrm{EW} = \mathrm{EW}_0(1+z)$) were selected as LAEs for the MB. For typical narrow band (NB), selected LAEs have an $\mathrm{EW}_0 > 25$ Å. However, for the narrow band filter NB392, selected LAEs have an $\mathrm{EW}_0 > 5$ Å. We refer to Sobral et al. (2018a) for the full selection criteria and further details regarding the SC4K LAEs.

The full SC4K catalogue contains 3908 sources with Lyα luminosities in the range $10^{(42.1-44.5)}$erg s^{-1}. We follow Calhau et al. (2020) and exclude the sources outside of the *Chandra* COSMOS Legacy Survey coverage, leaving us with a total sample of 3705 sources. This constitutes our sample of LAEs for analysis.

2.2   X-ray data: *Chandra* COSMOS-Legacy

The *Chandra* COSMOS-Legacy survey (Elvis et al. 2009; Civano et al. 2016) covers a total area of 2.2 square degrees across the COSMOS field. The exposure time of the survey varies according to region, with around 150 ks px^{-1} in the central-most 1.5 square degrees, dropping to 50 - 100 ks px^{-1} in the outer-most regions (Elvis et al. 2009; Civano et al. 2016). Specific exposure maps for each source were provided by J. Calhau, which allowed better error calculation for our X-ray fluxes.

The flux limits of the survey can be found in Civano et al. (2016).

2.3   Radio data: 1.4 GHz and 3 GHz VLA-COSMOS

The VLA-COSMOS Survey made use of the National Radio Astronomy Observatory's Very Large Array (VLA) to conduct wide-field imaging at the 1.4 GHz wavelength of the COSMOS field. Bondi et al. (2008) presents the catalogue of ~3600 radio sources detected in this band.

The VLA's 3 GHz COSMOS Large Project covers the entirety of the COSMOS field at a deeper sensitivity and higher resolution than the 1.4 GHz survey. Smolčić et al. (2017) presents this data in more detail as well as a catalogue of ~10000 radio sources in the 3 GHz band.

2.4   Obtaining Cutouts for Visual Classification

The images used in this work for visual classification were obtained using the freely available COSMOS Cutouts tool[1], which provides imaged fields with arcsecond diameters in the range 1" to 180". These images are provided by the

---

[1] https://irsa.ipac.caltech.edu/data/COSMOS/index_cutouts.html

COSMOS archive as part of the Cosmic Evolution Survey project, a survey designed to probe the formation and evolution of galaxies across cosmic time. The survey covers a targeted, 2 square degree equatorial field with imaging carried out in various wavelengths by most space-based as well as many ground-based telescopes.

In this paper we used images from the *Hubble Space Telescope (HST)* ($\lambda = 8140$ Å; Koekemoer et al. 2007), the *Chandra* X-ray Observatory ($\lambda = 2$ - 25 Å; Civano et al. 2016) and the VLA ($\lambda = 10$ cm, 20 cm; Smolčić et al. 2017).

3   METHODOLOGY

3.1   Identifying AGN sources

Images of the entire COSMOS field as seen by *Chandra* and the VLA were obtained. The *Chandra* images were subdivided into three wavebands: soft (0.5 - 2.0 keV), hard (2.0 - 7.0 keV) and full (0.5 - 7.0 keV). The VLA images were subdivided into 1.4 GHz and 3.0 GHz wavebands. We follow Sobral et al. (2018a) and Calhau et al. (2020) and create cutouts of each object to calculate their X-ray fluxes, X-ray luminosities and BHARs for the *Chandra* sources, and follow the same method to calculate 1.4 GHz and 3.0 GHz luminosities for the VLA sources, as detailed in Section 3.2. Exposure maps for each of the *Chandra* sources were provided by J. Calhau, allowing us to calculate more precise flux errors for our X-ray sources.

We follow Calhau et al. (2020) and consider a source as detected if its signal was greater than three times the noise value. An X-ray detected source is considered an AGN if its X-ray luminosity is in excess of 10^{42} erg s^{-1}. Such an X-ray luminosity would correspond to a star formation rate (SFR) within the galaxy of ~ 1000 M$_\odot$ yr^{-1} (Lehmer et al. 2016). Star formation at such a rate would only be found in the most active starburst galaxies (Sargsyan & Weedman 2009), and hence such sources are most likely AGN.

A radio detected source is considered an AGN if its radio luminosity is in excess of $10^{23.2}$ W Hz^{-1} (Meurs & Wilson 1984). Such a radio luminosity would correspond to a SFR within the galaxy in excess of ~ 100 M$_\odot$ yr^{-1}. Star formation at such a rate would only be found in the most active starburst galaxies (Sargsyan & Weedman 2009), and hence such sources are most likely AGN.

Out of all SC4K sources within the *Chandra* coverage, we find 258 sources at a signal to noise > 3 in the X-rays and 121 sources at a signal to noise > 3 in the radio, for a total of 322 sources which were subsequently marked as AGN. It is important to note that there is overlap in wavelength detection, with 57 sources detected in both X-ray and radio bands.

3.2   X-ray analysis

3.2.1   X-ray flux estimation

We follow the method outlined by Calhau et al. (2020) to convert count/s to flux. To do this the normalised count rate is multiplied by a conversion factor (CF), and divided by 10^{11}:

$$\mathrm{F_{x_0}} = (\mathrm{counts/s}) \times \mathrm{CF} \times 10^{-11}[\mathrm{erg\ s^{-1}cm^{-2}}] \qquad (2)$$

Conversion factors determined in Calhau et al. (2020) were used, and are the average values originally calculated in the C-COSMOS (see Elvis et al. 2009) and *Chandra* Legacy (see Civano et al. 2016) surveys. The conversion factors used were as follows:

$$\text{CF} = \begin{cases} 0.687, & \text{Soft band} \\ 3.05, & \text{Hard band} \\ 1.64, & \text{Full band} \end{cases} \tag{3}$$

We then apply an aperture correction of $A_c = 0.1$ calculated in Calhau et al. (2020) (which corrected the data to match Civano et al. (2016)). This allows the conversion of our aperture fluxes (F_{x_0}) to full fluxes (F_x):

$$\log_{10}(F_x) = \log_{10}(F_{x_0}) + A_c \tag{4}$$

3.2.2 X-ray luminosity estimation

Observed X-ray luminosity is calculated from full flux using:

$$L_x = 4\pi(F_x)d_L^2[\text{erg s}^{-1}] \tag{5}$$

where d_L is the luminosity distance in cm. Luminosity distance is calculated using our standard cosmology and redshift in TOPCAT (Taylor 2013).

Observed luminosity is then converted to rest-frame luminosity by multiplying it by the K-correction factor defined in Marchesi et al. (2016), producing:

$$L_{0.5\text{KeV}-10\text{Kev}} = \frac{L_x(10^{(2-\Gamma)} - 0.5^{(2-\Gamma)})}{(E_{\max}(1+z)^{(2-\Gamma)} - E_{\min}(1+z)^{(2-\Gamma)})} \tag{6}$$

such that z is the redshift and Γ is the photon index, assumed to be 1.4 (see Markevitch et al. 2003; Calhau et al. 2020, for motivation). $E_{\min}$ and $E_{\max}$ are band specific and are determined by *Chandra*, they have values:

$$E_{\min} - E_{\max} = \begin{cases} 0.5 - 2.0[KeV], & \text{Soft band} \\ 2.0 - 7.0[KeV], & \text{Hard band} \\ 0.5 - 7.0[KeV], & \text{Full band} \end{cases} \tag{7}$$

3.2.3 X-ray Black Hole Accretion Rate

To determine BHAR we must first determine the bolometric luminosity, using:

$$L_{\text{bol}} = 22.4 \times L_{0.5\text{KeV}-10\text{KeV}} \tag{8}$$

where 22.4 is the bolometric conversion factor found in Calhau et al. (2020), and originally calculated in Lehmer et al. (2013) as a median value for AGN with $L_x = 10^{41} - 10^{46}$ [erg s^{-1}]. As stated in Calhau et al. (2020) a median value of 22.4 is used for simplicity, despite the inherent accuracy limitations.

BHAR is then estimated using:

$$\dot{M}_{\text{BH}} = \frac{L_{\text{bol}}(1-\epsilon)}{\epsilon c^2} \times 1.59 \times 10^{-26}[\text{M}_\odot\text{yr}^{-1}] \tag{9}$$

where $\dot{M}_{\text{BH}}$ is the BHAR, ϵ is the accretion efficiency assumed to be 0.1 (see Soltan 1982; Fabian & Iwasawa 1999; Marconi et al. 2004, for motivation), and c is the speed of light.

3.3 Radio analysis

3.3.1 Radio flux estimation

To determine the full radio flux (F_ν), we use:

$$\log_{10}(F_\nu) = \log_{10}(F_{\nu_0}) + A_c \tag{10}$$

We use the same apertures as Calhau et al. (2020), and hence the following aperture corrections are used:

$$A_c = \begin{cases} -0.05, & 3.0 \text{ GHz} \\ 0, & 1.4 \text{ GHz} \end{cases} \tag{11}$$

These aperture corrections determined in Calhau et al. (2020) are found by comparison with Smolčić et al. (2017) for 3.0 GHz and Bondi et al. (2008) for 1.4 GHz.

3.3.2 Radio luminosity estimation

The radio luminosity is estimated using:

$$L_\nu = \frac{4\pi d_L^2}{(1+z)^{(\alpha+1)}} F_\nu \tag{12}$$

where:

$$\alpha = \frac{\log_{10}\left(\frac{F_3}{F_{1.4}}\right)}{\log_{10}\left(\frac{3.0}{1.4}\right)} \tag{13}$$

such that d_L is the luminosity distance in meters, z is the redshift, α is the spectral index and F_ν is the flux for 1.4 GHz or 3.0 GHz [WHz^{-1}m^{-2}]. Following Calhau et al. (2020), we set our spectral index, α to -0.8.

3.3.3 Radio frequency conversion

To allow comparisons of all our radio sources, we convert 3.0 GHz luminosity to 1.4 GHz, using:

$$L_{1.4\text{GHz}} = \frac{4\pi d_L^2}{(1+z)^{\alpha+1}} \left(\frac{1.4}{3.0}\right)^\alpha F_{3.0\text{GHz}}[\text{WHz}^{-1}] \tag{14}$$

where d_L is the luminosity distance in meters, α is the spectral index (assumed to be -0.8) and $F_{3.0\text{GHz}}$ is the flux in the 3.0 GHz band [WHz^{-1}m^{-2}]. Hereafter $L_{1.4\text{GHz}}$, refers to 1.4 GHz data, and converted 3.0 GHz data (when the radio source was undetected in the 1.4 GHz band).

3.3.4 Radio Black Hole Accretion Rate

In this work we present the first direct comparison between X-ray and radio BHARs.

To determine the radio BHAR, we use:

$$\dot{M}_{\text{BH}} \approx 4 \times 10^7 \left(\frac{L_{1.4\text{GHz}}}{10^{30}\text{ergs}^{-1}}\right) \times 1.59 \times 10^{-26}[\text{M}_\odot\text{yr}^{-1}] \tag{15}$$

from Körding et al. (2006). Körding et al. (2006) and Körding et al. (2008) state that the approximate accretion rate for hard state X-ray binary (XRB) systems and unbeamed AGN can be calculated in the above way using the core radio luminosity.

As stated in Körding et al. (2008), this equation is normalised using XRBs and as such when the relation is extrapolated to more complicated AGN systems the uncertainty inherently increases, and the fluxes may be slightly underestimated. The specifics of the normalisation and bolometric corrections adopted are discussed in Körding et al. (2006).

3.4 Morphologies

We produced a set of 2" by 2" images of the sources that were detected in the X-ray and radio using the *HST*-ACS Tiles setting on the COSMOS Cutouts tool as described in Section 2.4. These images were obtained using *Hubble*'s Advanced Camera for Surveys (ACS). Not all of the sources lie within the *HST* field, leaving 48 X-ray and 19 radio AGN sources that we did not have images for. We considered classifying these sources using the X-ray and radio images, however these images are in different wavelengths to the *HST* images which would result in inconsistent classification.

The variety of telescopes used to survey the COSMOS field means we could have used optical images from the Subaru telescope to classify these missing sources. However, as Subaru is a ground-based telescope and *HST* is space-based this would increase the likelihood of inconsistent classification.

We adopted a morphology classification scheme following Paulino-Afonso et al. (2018) and Barlow-Hall et al. (2019): Type 0: Point like, a single source with no significant halo or extension. Type 1: Compact, a circular, extended source. Type 2: Disky, an extended ovular or 'cigar' shaped source. Type 3: Irregular, an obscurely shaped source or one with multiple bright points visible. Type 4: Unclassifiable, a source that we do not have a *HST* image for, or a source not visible in the *HST* image. Examples of each type can be seen in Figure 1. All sources given a Type 4 classification were discarded when investigating morphology.

Four independent parties classified each source to avoid bias. The images were opened in SAOImageDS9 using the same viewing settings to ensure consistency. Where there was disagreement over the classification of an individual source the mode classification was chosen. We decided that it would not be sensible to take a mean value for the classification since there were a number of sources that were given point-like or compact by one classifier and unclassifiable by another. In cases like these, taking a mean would result in a disky classification, however the source had not be classified as such by any individual.

When analysing the morphology relations we discount the unclassifiable sources as they tell us nothing about the galaxy's morphology. Unclassifiable sources are still considered when considering BHAR analysis, as these sources have been detected by *Chandra* and/or the VLA and hence accurate BHARs can still be calculated for them. We also found it fitting in many cases to combine point-like and compact sources into one category for analysis, since we suspect many point-like sources are simply faint compact sources.
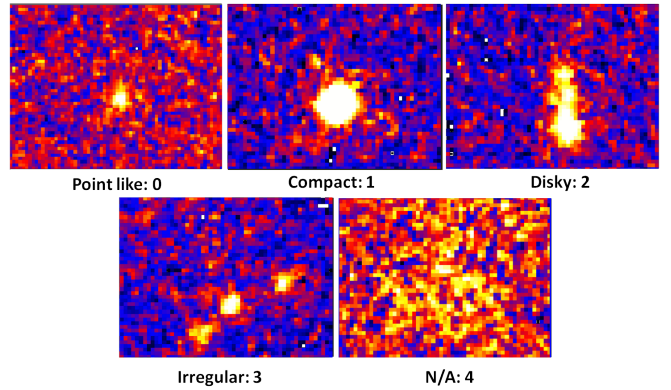
Figure 1. Example 2" x 2" cutouts and the values we would assign using our visual classification scheme, as described in Section 3.4. In this example, the Type 4 classification is a cutout where an image was taken by the HST, but no galaxy is clearly visible. In other cases no image was taken by the *HST* and so these galaxies were automatically classified as Type 4.

4 RESULTS

4.1 AGN

Of the 3705 LAEs in the SC4K catalogue considered here we find 322 AGN, representing 8.7±0.5% of the total sources considered. 258 of these sources are detected in the X-ray by *Chandra*, 121 are detected in radio by the VLA and 57 are detected in both bands.

Considering only the sources with classifiable morphologies this number is reduced to 232 AGN, 192 in the X-ray, 90 in the radio and 50 detected in both bands.

For the X-ray sources the calculated luminosities fell in the range of $\sim 10^{43}$ erg s^{-1} to $\sim 10^{45}$ erg s^{-1}, in broad agreement with those calculated in Calhau et al. (2020). These luminosities corresponded to X-ray calculated BHARs ranging from ~ 0.07 M$_\odot$ yr^{-1} to ~ 23 M$_\odot$ yr^{-1}, indicating a highly varied sample, with some very active AGN detected.

The radio calculated BHARs ranged from ~ 0.09 M$_\odot$ yr^{-1} to ~ 8.8 M$_\odot$ yr^{-1}. This broadly traces the same range as the X-ray calculated BHARs, indicating that the Körding et al. (2006) relation may be accurate. We will further explore this when we directly compare X-ray and radio BHARs in Section 4.5.3.

4.2 Comparison with Calhau et al. (2020)

Figure 2 shows a plot of our calculated X-ray BHAR vs. those from the Calhau et al. (2020) paper. As can be seen there is a clear, direct correlation between our results and those of the Calhau et al. (2020) data, meaning our results are in excellent agreement.

4.3 Morphologies

4.3.1 Visual classifications

Of the 322 total AGN sources, 57 of which are detected in both X-ray and radio, there are 232 classifiable sources. Most of the AGN are classified as compact in the rest-frame UV (see Table 2 for percentage distributions). The next most

Selection filter	Lyα redshift	# LAE candidates	X-ray only detected sources	Radio only detected sources	AGNs detected
IA427	2.51151	711	43	27	56
IA464	2.81579	292	19	13	27
IA484	2.98026	679	62	29	75
IA505	3.15296	463	40	13	47
IA527	3.33388	610	39	15	49
IA574	3.72039	96	6	6	10
IA624	4.13158	133	1	3	3
IA679	4.58388	74	2	3	4
IA709	4.83059	77	2	2	4
IA738	5.06908	72	4	1	4
IA767	5.30757	27	3	0	3
IA827	5.80099	32	0	0	0
NB392	2.22368	140	21	6	23
NB501	3.12007	44	7	2	7
NB711	4.84704	73	3	1	4
NB816	5.71053	182	6	0	6
Total:		3705	258	121	322

Table 1. The full SC4K sample used in this work. Including data from 12 medium-bands and 4 narrow-bands. These 16 filters sliced the whole SC4K sample by redshift from $z \sim 2$-6. The table shows the redshift distribution of the whole sample and X-ray and Radio sources.
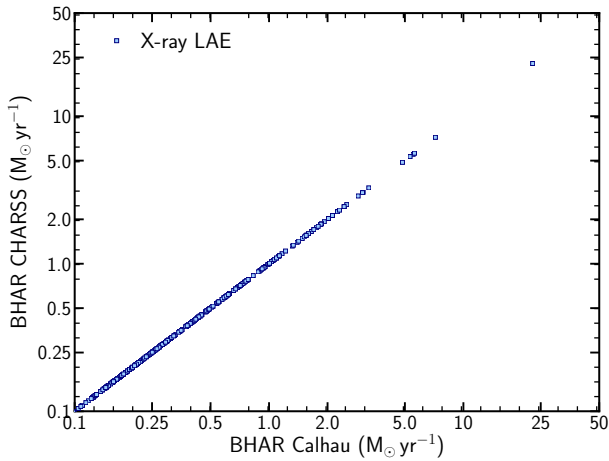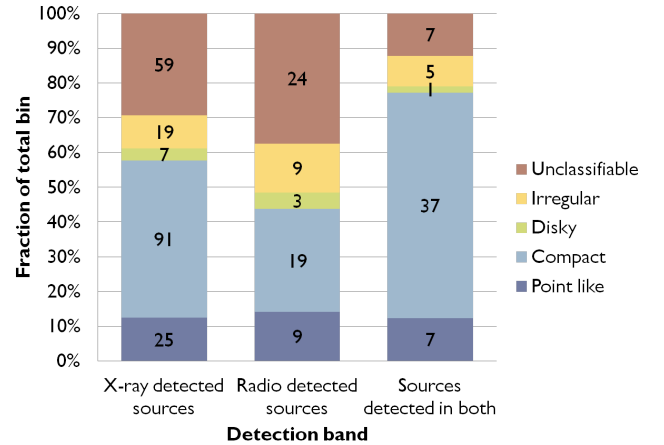

Figure 2. X-ray accretion rate data calculated by our program plotted against the values calculated by Calhau et al. (2020). All the data follow a $y = x$ line showing that our values are in perfect agreement with previous studies.

Figure 3. Morphology types of our AGN sources, separated by band detection and colour-coded by morphological type. The numbers on each column block represent the number of sources of that morphological type detected in that band.

common type, other than the unclassifiable sources, is point-like. Point-like sources are similar to compact in their shape; they are both rounded, with point-like being smaller than compact. Very few SC4K AGN are classified as disky.

As shown in Figure 3, when separating the sources by the waveband they are detected in we find similar trends as when considering the sample as a whole. Most are compact or point-like sources, with almost no disky or irregular sources present. Unclassifiable sources make up a reasonably significant proportion of all sources regardless of detection band (29±3% in the X-ray, 38±6% in the radio).

When considering the sources only detected in a single band (X-ray or radio), over 40% of the sources are compact or point-like, with similar small percentages of irregular and

disky sources. However, we note there are far more compact sources detected in the X-ray than in the radio.

The 57 sources detected in both X-ray and radio are overwhelmingly compact or point-like (see Figure 3), with these two classifications representing over 70% of these sources. There are almost no disky sources and, interestingly a significantly smaller percentage of unclassifiable sources compared to sources detected in only one waveband.

We postulate that as these sources are detected by both *Chandra* and the VLA they must be quite luminous, and hence are more likely to appear in *HST* images.

Morphology	X-ray only detected sources	Radio only detected sources	X-ray and radio detected sources	Percentage of all sources (%)
Point like	25	9	7	$13 \pm 2\%$
Compact	91	19	37	$46 \pm 3\%$
Disky	7	3	1	$3 \pm 1\%$
Irregular	19	9	5	$10 \pm 2\%$
Unclassifiable	59	24	7	$28 \pm 3\%$
Total	201	64	57	100% (322 sources)

Table 2. The distribution of the different types of sources in the data. The first two columns represent the sources that were only detected in the X-ray and the radio respectively, these do not include the sources that are detected in both bands.
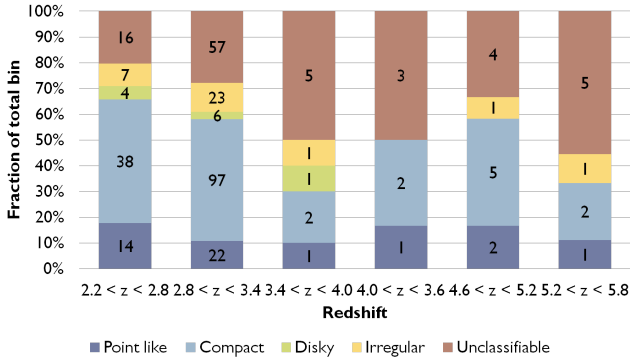
Figure 4. Morphology types of our AGN sources (X-ray or radio detected) within each of the six redshift bins used in this study. Morphologies are colour-coded, and the numbers on each column represent the number of sources of that morphological type detected at that redshift.

4.3.2 Morphology vs. Redshift

In Figure 4 we can see similar trends to those discussed in Section 4.3.1. A significant proportion of all sources are compact and point-like regardless of redshift. There seems to be little evolution of morphology across redshift, although the plot suggests that there are no disky sources among our SC4K AGN sample at redshifts higher than $z \sim 4$. While this is true within our sample, it should be noted that the vast majority of sources are in the first two redshift bins, with far fewer sources in the final four redshift bins, meaning these bins are likely less representative of the actual sources at these redshifts.

4.3.3 Morphology vs. Lyα luminosity

In order to investigate a possible selection bias based upon luminosity at high redshift, we decided to bin our sources based on their Lyα luminosity and compare this to their associated redshift.

Lyα luminosity was used to compare the AGN sources as it had not been used to calculate BHARs unlike X-ray or radio luminosity, and most importantly because the SC4K sample is Lyα selected.

We created five bins of width 0.5 dex in Lyα luminosity ranging from $10^{42.1} - 10^{44.6}$ erg s^{-1}. At lower Lyα luminosity, there is no correlation between Lyα luminosity and morphology. The least luminous bin (of Lyα luminosity $= 10^{42.1} - 10^{42.6}$ erg s^{-1}) contains only 17 sources, and so

is not considered representative enough to make significant conclusions.

The second least luminous bin (of Lyα luminosity $= 10^{42.6} - 10^{43.1}$ erg s^{-1}), which contains 160 AGN sources, shows a larger than normal fraction of point-like sources when compared to the data-set as a whole. For this bin 27% of the classifiable sources are point-like, compared to $18 \pm 3\%$ for the whole sample. There is also a lower than average fraction of compact sources, 48% compared to $63 \pm 3\%$ for the whole sample. We hypothesise that less luminous sources will appear smaller in *HST* images and are therefore more likely to be classified as point-like than compact.

All classifiable sources above a Lyα luminosity of $10^{43.6}$erg s^{-1} are compact sources. This could indicate that highly luminous AGN host galaxies are more likely to have compact morphologies.

In order to explore this theory we looked at the binned sources in terms of a fraction of the total sample. Out of all the AGN, 232 are classifiable sources with a further $63 \pm 3\%$ of these sources classified as compact. The top two most luminous bins of Lyα luminosity, which represent sources with luminosity greater than $10^{43.6}$erg s^{-1}, contain only 19% of the classifiable AGN. As such, these bins contain contain too few sources to draw significant conclusions, and we find it likely that the presence of such a high fraction of compact sources in these bins is a reflection of the overall surplus of compact sources found in our sample.

Further study of the morphologies of the most luminous Lyα selected AGN would help to shed more light on if they have a preferred morphological type.

4.4 BHAR vs. Lyα luminosity

Figure 5 shows X-ray BHAR against redshift, with each point colour-coded according to its Lyα luminosity. We find that the most luminous sources (shown in red) are found at lower redshifts, between $z \sim 2.5$ - 3.5, with high redshift sources having fairly typical luminosities within our data set. This implies there is no significant selection bias at high redshift, and that high redshift sources should not have abnormally high BHARs that would skew our data.

We postulate then that the reason our number of detections decreases at high redshift is due to increasing noise levels, meaning fewer sources meet the 3σ limit to qualify as a detected source. Furthermore, Figure 6 seems to show some correlation between Lyα emission and X-ray BHAR, albeit with a high degree of scatter evident. This is the rela-
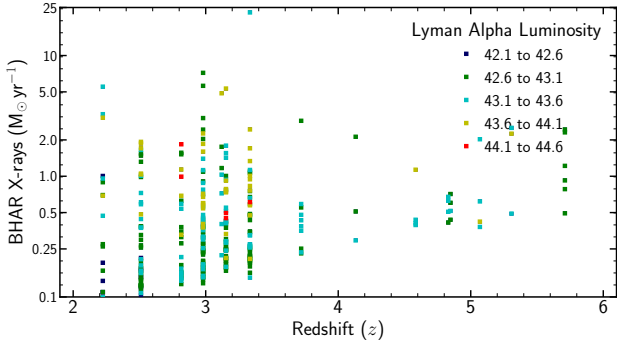
Figure 5. X-ray BHAR plotted against redshift, with the Lyα luminosity of each source colour-coded according to each luminosity bin. High luminosity sources (in red) are found at low redshifts, indicating there is no luminosity selection bias at high redshift.
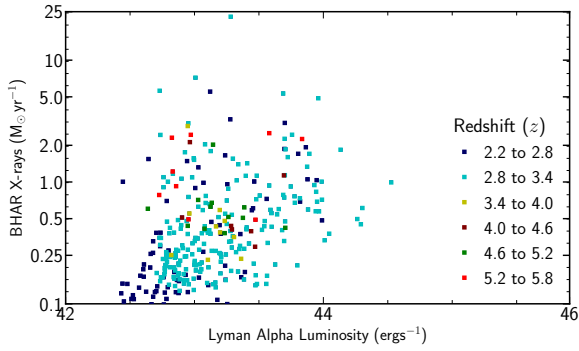
Figure 6. X-ray BHAR plotted against Lyα luminosity, with the redshift of each source colour-coded according to each redshift bin. There appears to be some correlation between BHAR and Lyα luminosity. This relationship is also found and discussed in more detail in Calhau et al. (2020).

tion already found, presented and discussed in Calhau et al. (2020).

4.5 Black Hole Accretion Rates (BHARs)

4.5.1 BHAR vs. Morphology

Figures 7 and 8 show X-ray and radio accretion rates plotted against the morphologies of the sources within SC4K. The sources are separated into five separate bins of morphology. Colour-coded symbols denote the median BHAR value for each morphology and are plotted at the centre of each bin.

What is immediately clear is that Radio and X-ray BHARs broadly trace each other, with no significant discrepancies.

Within the X-ray data there seems to be some correlation between BHAR and morphology, as compact sources have the highest accretion rates. However, when considering the radio BHARs, compact sources have the lowest accretion rates of any morphology, albeit marginally, and the overall relation for the radio is remarkably flat (Figure 8).
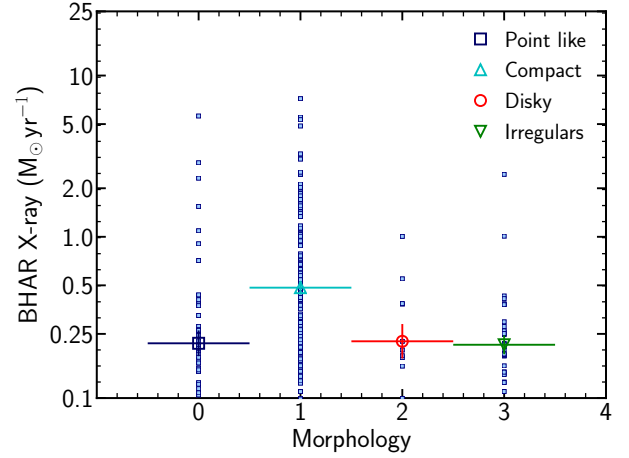
Figure 7. X-ray BHAR plotted against morphology for all the AGN sources. The morphological type of each source is colour-coded and symbolically indicated. Compact sources appear to have the highest BHARs of any morphological type by a factor of ∼ 2.
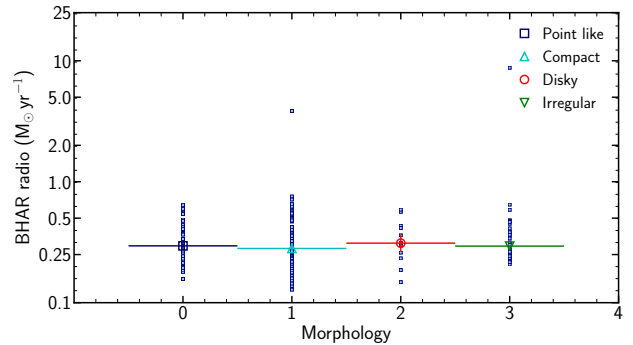

Figure 8. Radio BHAR plotted against morphology for all the AGN sources. The morphological type of each source is colour-coded and symbolically indicated. Compact sources appear to have the lowest accretion rates of any morphological type, albeit very marginally. Overall the relation is remarkably flat.

4.5.2 BHAR vs. Redshift

Figure 9 shows the X-ray (in blue) and radio (in red) accretion rates plotted against redshift. The sources are separated into 6 separate bins of width $\Delta z = 0.6$ from $z = 2.2 - 5.8$. Symbols denote the median BHAR value for each each morphological type within each bin. Radio data has been given a +0.5 shift from the centre of the bin and X-ray data has been given a -0.5 shift from the centre of the bin in order to aid visual interpretation. Here, point-like and compact sources are combined into a single bin, this is due to the likelihood of faint compact sources being classified as point-like, and also for simplicity.

As with the morphology plots, it is immediately clear that radio accretion rates broadly trace the X-ray accretion rates at all redshifts. At high redshift however it appears the
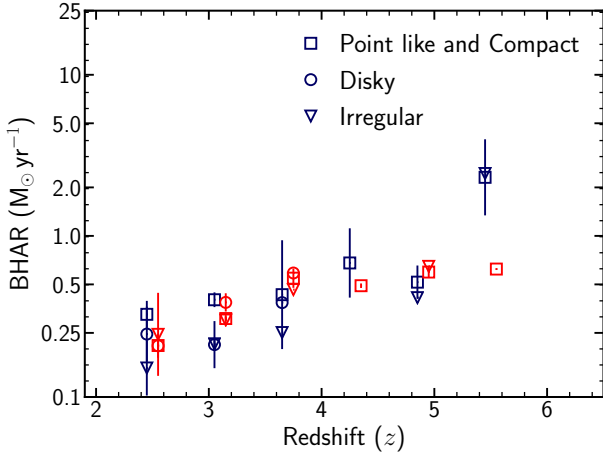
Figure 9. X-ray and radio calculated BHAR against redshift with bins of morphology shown. X-ray data appears in blue and radio data appears in red. The morphological types of the sources are symbolically indicated, point-like and compact sources are combined into a single bin here. The radio data has been given a +0.5 shift along the x-axis and the X-ray data has been given a -0.5 shift along the x-axis in order to aid visual interpretation. For the X-ray data it appears point-like and compact sources dominate the BHAR in every redshift bin. For the radio data there is no clear consistently dominating morphology.

X-ray data continues its upward trend, while the radio data flattens out.

Considering only the X-ray data, it seems clear that point-like and compact sources dominate the BHARs in every redshift bin. However, as with morphology data, the radio disagrees. In this plot, irregular sources dominate the BHAR between $z = 2 - 3$, with disky sources dominating between $z = 3 - 4$. At high redshift there is no consistent dominating morphology.

It is worth noting in these high redshift bins that there are significantly lower numbers of sources, meaning some bins do not contain any of some morphological types. This especially affects the disky morphology which has a disproportionately low number of sources across all redshifts.

Figure 10 shows a similar plot in which each bin only has a single symbol denoting the median value of the entire bin, with no separation by morphological type. X-ray remains in blue and radio remains in red. The same shifts are used to aid visual interpretation.

The X-ray BHARs show a characteristic peak between $z = 2-3$, indicating a high level of black hole activity in this redshift range, which is in agreement with the theory that the overall BHAR of the Universe peaks between $z = 1 - 3$ (Nandra 2009; Brandt & Alexander 2010; Delvecchio et al. 2014). This peak is not present however when considering the radio. Both plots show an increase in BHAR with increasing redshift.

What is also interesting is the scatter of the individual BHARs for each waveband. Radio calculated BHARs follow the median for each bin much more strongly than X-ray calculated BHARs. This could be an indication of the highly variable nature of AGN sources, with radio tracing much
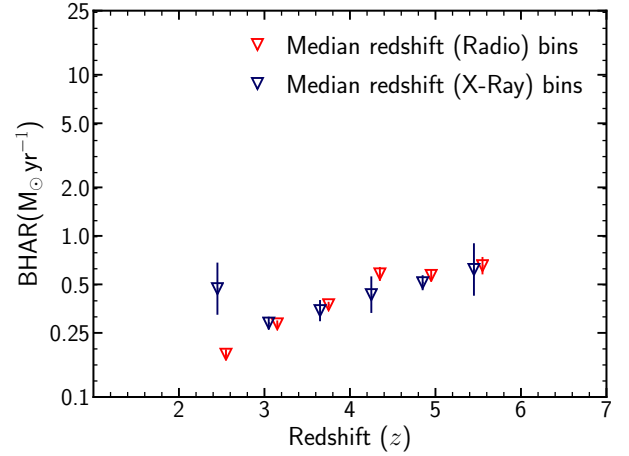
Figure 10. X-ray and radio calculated BHAR against redshift with the median value for each redshift bin shown. X-ray appears in blue and radio appears in red. Here there is no separation by morphological type within each bin. The radio has been given a +0.5 shift along the x-axis and the X-ray has been given a -0.5 shift along the x-axis in order to aid visual interpretation. The X-ray data shows a peak between $z = 2 - 3$, consistent with the literature. Both data indicate an increasing BHAR with increasing redshift.

longer timescales than the X-ray and hence showing more stability.

4.5.3   X-ray vs. Radio calculated BHAR

Figure 11 shows a plot of X-ray BHAR against radio BHAR for the 57 AGN that were detected in both X-ray and radio wavebands with a line of $y = x$ added. Sources with compact or point-like morphologies are denoted with a black halo. As mentioned in Section 4.3.1, the majority of sources detected in both bands had compact or point-like morphologies.

The plot shows no correlation between X-ray and radio BHAR, with a large amount of scatter evident about the line of $y = x$. The X-ray BHARs show the largest range by far, spanning approximately two orders of magnitude from ~ 0.1 $M_\odot$ yr^{-1} to ~ 10 $M_\odot$ yr^{-1}. The radio is far less variable, spanning only a single order of magnitude from ~ 0.1 $M_\odot$ yr^{-1} to ~ 1 $M_\odot$ yr^{-1}.

The lack of a tight correlation is potentially indicative that AGN systems are highly variable by their nature (as mentioned in Section 4.5.2). Due to the different timescales involved we might expect that the radio accretion rate is more indicative of the typical accretion rate of the source over a long time. We hypothesise that sources with 1:1 correlation potentially have a much more stable BHAR history, while those that deviate are likely the most variable.

5   DISCUSSION

5.1   Morphologies

Across the entire sample of SC4K AGN we find a surplus of compact and point-like sources. The proportions of these
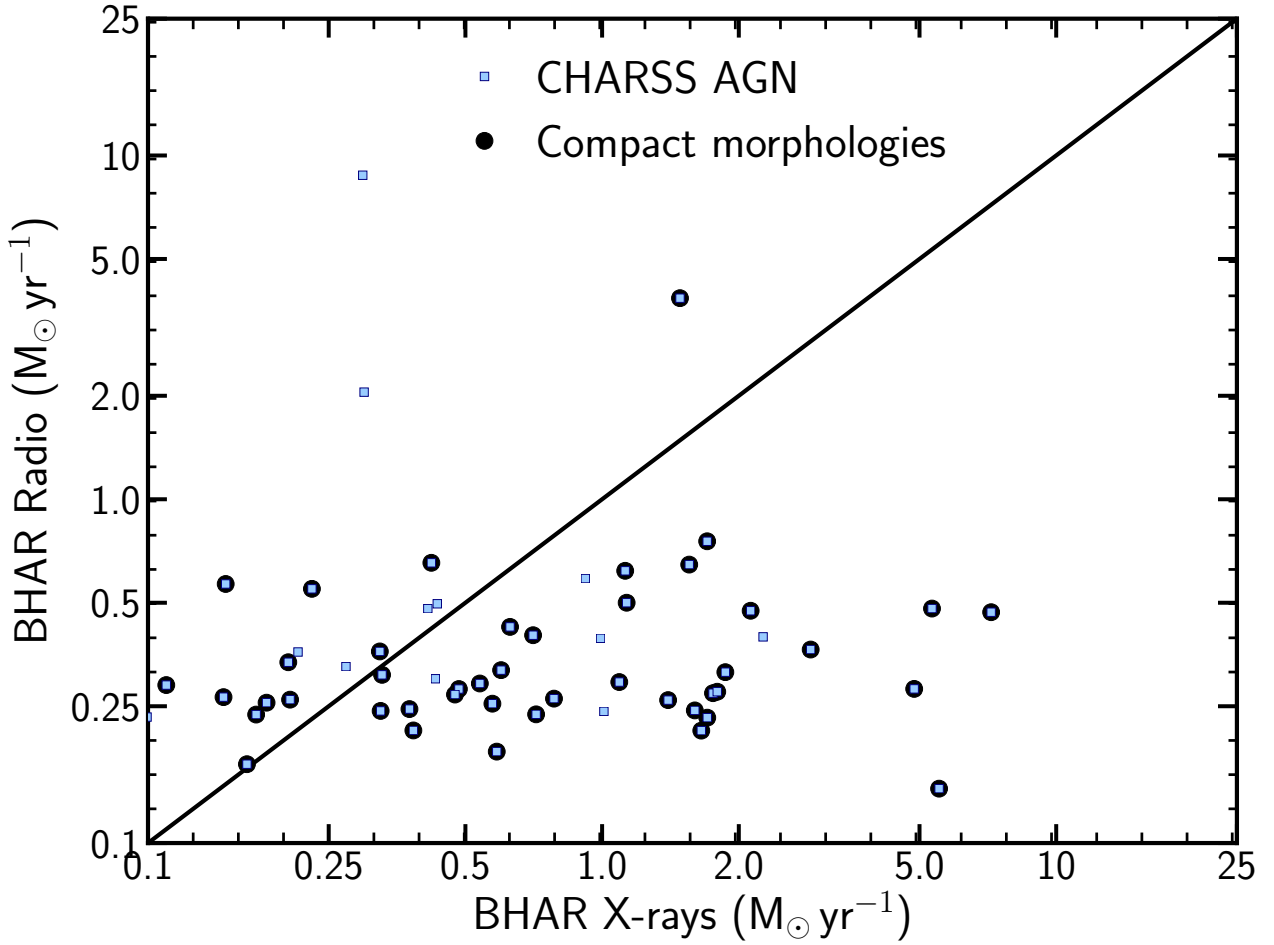
Figure 11. X-ray calculated BHAR against Radio calculated BHAR for the 57 AGN detected in both bands. A line of $y = x$ has been added and sources with compact or point-like morphologies are highlighted with a black halo. There appears to be very little tight correlation, as may be expected due to the variability of the X-ray. Sources that lie on or near the line of $y = x$ are expected to have stable accretion rate histories. The accretion rate trend appears very flat in the radio.

sources remain roughly constant across every redshift bin, and they represent the majority of classifiable sources, at over 60% in every bin. Paulino-Afonso et al. (2018) also find that the majority of bright sources within the COSMOS field are compact in nature, with small numbers of disky or irregular sources at high redshift.

Barlow-Hall et al. (2019) consider all LAEs within SC4K and find that the majority of sources are compact or disky. Of the 303 AGN they detect, most were compact or point-like in nature, and hence AGN are less likely to be disky sources when compared with the full SC4K sample. When considering the radio detected AGN sources, the most common morphological type was point-like which is not in agreement with our findings. This is likely due to differences in our classification methods, specifically with regards to point-like sources. In many cases we have combined the point-like and compact sources for analysis, as we believe they represent similar structures.

Furthermore, the nature of the classification system adopted is highly subjective, and while every care has been taken to ensure consistent classification discrepancies may still arise.

Our AGN are typically very luminous with X-ray luminosities in excess of 10^{43} erg s^{-1}. As such, we hypothesise that the reason such a high percentage of our AGN are given compact and point-like classifications is due to the highly-luminous accretion disk of the central SMBH outshining the entire galaxy. In this case we would instead be classifying the morphology of the SMBH-accretion disk system, which are almost exclusively point-like in their nature.

We also note that compact and point-like sources may be the same sources but with different brightnesses.

5.2 Black Hole Accretion Rates (BHARs)

5.2.1 BHAR vs. Morphology

We find in the X-ray data that compact sources have the highest accretion rates of any given morphology. This is consistent with results in the literature. Barlow-Hall et al. (2019) find within SC4K that the half light radii of AGN decrease with increasing BHAR, indicating that compact and point-like sources have the highest accretion rates of any morphology. As previously stated we hypothesise that these high luminosity sources have actually been classified based upon the shape of their central SMBH-accretion disk system, rather than on the morphology of the entire galaxy.

We also hypothesise that the more compact sources may have smaller, denser accretion disks which may allow for faster and more efficient accretion when compared to more extended disky sources. While this may be true in reality, the limitation of *HST*'s Advanced Camera for Surveys (ACS) instrumentation makes it difficult for us to draw meaningful conclusions in this regard. The ACS can resolve down to 0.05". At a redshift of $z = 2.2$, 0.05" would correspond to a distance of 420 pc. Previous studies have found that the typical width of an AGN or Quasar accretion disk ranges from 5-10 light days, or approximately 10^{-2} pc (see Hawkins 2007). As such, *HST*'s ACS does not have the resolving capability to image the accretion disk directly, and so large or small accretion disks will still appear compact in the *HST* ACS images.

Hence, it seems more likely that disky sources instead host less active AGN which do not outshine the entire galaxy to the same extent as point-like or compact sources.

More analysis in this area, observing and classifying the morphology of the galaxies in different wavebands may help to provide more concrete classifications, and give a better indication of the morphological nature of the galaxy as a whole, rather than our picture being dominated by the emission from the central SMBH with regard to compact and point-like sources.

We note that the radio data provides a very different picture, with disky sources dominating the BHARs at lower redshifts and irregular sources dominating at higher redshifts. This may be due to the source of the emission. If our hypothesis regarding the disky sources is correct, and they host less active AGN, it may be possible that our radio data is contaminated with emission from star formation. This would lead to us recording higher emissions than those from the AGN radio core which would in turn lead to inflated BHARs. It is also possible that the radio emission is simply tracing past AGN activity.

Delvecchio et al. (2018) consider SMBH accretion in radio selected AGN out to $z \sim 4$ using the same data from the VLA-COSMOS 3 GHz Large Project as this work. They note that as radio emission may arise from processes related to both star formation and AGN activity they use the infrared radio correlation (IRRC; see e.g. Delhaize et al. 2017) to decompose the radio emission of their sources and isolate the emission caused only by AGN activity. In future it may be useful to use this same relation to decompose the radio emission of our disky sources, in order to investigate whether our data has indeed been contaminated by star formation.

5.2.2 BHAR vs. Redshift

In the X-ray we find a peak in BHAR between $z = 2 - 3$ which is consistent with the literature (Nandra 2009; Brandt & Alexander 2010; Delvecchio et al. 2014). This is further evidence that the black-hole activity of the Universe peaks between $z = 1 - 3$. The limits of this redshift peak appear to change slightly dependent on the wavebands used for analysis, with Delvecchio et al. (2014) using IR and finding a value of $z \sim 2$ and Aird et al. (2010) using X-ray and finding a value of $z \sim 1.2$. As our data does not extend any further towards the present than $z = 2.2$ we are confident our value is consistent with the literature, and our results here are broadly comparable to those found by Calhau et al. (2020) using the same data-set.

For both X-ray and radio data we observe a a slight increase in BHAR for increasing redshift, consistent with Calhau et al. (2017, 2020), although our results seem to plateau at higher redshifts of $z > 4$.

We postulated that this increased BHAR at higher redshift may be due to anti-hierarchical growth. Observations suggest that high mass black holes existed far earlier than expected in the Universe, and that these high mass black holes accreted the majority of their mass at high redshift (see e.g. Merloni 2004; Hirschmann et al. 2012). This relation is found in almost all wavebands including Optical: Cristiani et al. (2004); Wolf et al. (2003) and NIR: Matute et al. (2006).

However, it is far more likely that the observed upwards trend is due to the 3σ detection limit used in this work (see Barlow-Hall et al. 2019; Calhau et al. 2020, for motivation). At high redshift the noisier sources may be excluded, and hence our sample beyond a redshift of $z \sim 3.5 - 4$ is likely much less representative of the global AGN fraction. This is further evidenced by the lack of sources (37 detected) above $z \sim 3.5$.

When considering the luminosity of the sources we find no evidence for a strong selection bias at high redshift, with our highest luminosity sources being found between $z \sim 2.5 - 3.5$ as shown in Figure 5. This is further evidence for the argument that the reason for the decline in the number of sources at high redshift is less due to the low luminosity of these sources and more to do with the high levels of noise in the data at these redshifts, as we still detect low luminosity sources even at $z \sim 6$. This hypothesis is also supported by the increasing fraction of unclassifiable sources at high redshift, showing the effect of noise is not limited to radio or X-ray bands but also extends to the optical wavelengths probed by *HST*.

Figure 6 also implies correlation between Lyα luminosity and X-ray BHAR, similar to that found in Sobral et al. (2018b) and directly by Calhau et al. (2020), which is further evidence that the activity of AGN is also traced by Lyα emission. There is a high degree of scatter evident in this plot however, indicating the high variability of AGN when observed in the X-ray, or the complicated nature of Lyα radiative transfer.

5.2.3 X-ray vs. Radio BHAR

Figure 11 seems to suggest little to no relation between X-ray and radio calculated BHARs, with X-ray calculated BHARs

spanning a significantly larger range than radio calculated BHARs. This observation is also clear when comparing individual BHARs to the median bin values in Figure 10. The radio sources show far less scatter at all redshift, and follow the median bins values much more closely than the X-ray sources. This may be evidence for the stability and longer timescale of radio emission. Calhau et al. (2017) finds radio emission lasts on the order of ~ 100 Myr, and as such may be less susceptible to short-term variation than X-ray accretion rates. As such, we postulate that radio calculated BHARs may be better than X-ray at tracing the accretion rate of a specific source over a far longer timescale.

The large scatter in X-ray is likely due to a number factors, chiefly the high variability of AGN sources (e.g. Angione 1973). We also refer to Körding et al. (2006, 2008) which states that the method used in this work as detailed in Section 3.2 may underestimate the radio fluxes and, by extension, BHARs for our radio sources. As such, there may be systematic errors that are not fully accounted for here that could bring the radio scatter more in line with that displayed in the X-ray.

The discrepancy between X-ray and radio data may also be accounted for by the periodic behaviour of AGN sources. AGN variability has been studied in many wavebands including Optical: Angione (1973), X-ray: Marshall et al. (1981) and NIR: Neugebauer et al. (1989). The timescale of the variation is known to increase as the observation wavelength increases, with X-ray variability observable over minutes or hours, optical variability observable over days to months and NIR variability observable over months or years (Elmer et al. 2020). The reason for these variations is unknown, however if this clear trend is continued at longer wavelengths then this would explain the reduced variability seen in our radio sources.

As such, we suggest that radio calculated BHARs may provide a lower limit to the BHAR of a given source over a long timescale, and vary significantly less than X-ray calculated BHARs. Hence, this may make radio data far more reliable measures of the BHARs of AGN than X-ray. Furthermore, it may also be a promising way of identifying the most and least variable AGN as those with large and small X-ray vs. radio BHAR disagreement respectively.

6 CONCLUSIONS

In this paper we identify Active Galactic Nuclei (AGN) sources in the SC4K catalogue of 3705 Lyα emitters (LAEs) from redshift $z \sim 2 - 6$. We calculate black hole accretion rates (BHARs) using radio data from two VLA-COSMOS Surveys and X-ray data from the *Chandra* COSMOS Legacy survey, in order to explore how BHARs change across cosmic time. We also determine the rest-frame UV morphologies of these LAE AGN and their relationship to both BHARs and redshift. Our main results are:

• We detect 322 AGN in the sample of 3705 LAEs, representing 8.7±0.5% of the sources.

• 258 AGN are detected in the X-ray, 121 are detected in the radio and 57 are detected in both bands.

• There are 232 AGN with classifiable morphologies in the rest-frame UV, 50 of which are detected in both X-ray and

radio. Sources detected in both bands have a lower proportion of unclassifiable sources (12±4% compared to 38±6% of the radio only and 29±3% of the X-ray only detected sources).

• The AGN sources in SC4K are mainly compact type sources in the rest-frame UV, making up 63±3% of the classifiable AGN, consistent with the literature.

• Most sources are found between $z = 2.2 - 3.4$ when binned by redshift.

• X-ray BHARs peak at $z \sim 3$, consistent with the literature, and range from ~ 0.07 M$_\odot$ yr^{-1} to ~ 22 M$_\odot$ yr^{-1}. Compact sources seem to have the highest BHARs for X-ray detections.

• Radio BHARs range from ~ 0.09 M$_\odot$ yr^{-1} to ~ 8.8 M$_\odot$ yr^{-1}. Point-like and compact sources seem to have the lowest BHARs, with disky sources having the highest BHARs at low redshift for radio detections.

• Lyα luminosity appears to broadly trace X-ray calculated BHARs, consistent with the literature.

• We find radio BHARs are broadly in agreement with X-ray BHARs, implying that the Körding et al. (2006) relation is likely accurate and might be used (see Section 5.2.3).

• Radio BHARs show less scatter than X-ray BHARs, indicating that radio is a more stable and reliable measure of the lower limit of BHARs of AGN than X-ray.

The LAEs in the SC4K sample provide numerous AGN for study across a vast range of redshift. As the sample is not AGN selected, we find an exceptionally diverse population of sources. Further investigation into the radio relation for obtaining BHARs of AGN would be highly useful in confirming the accuracy of this method for a wide variety of sources. Further comparison with the literature would also help to confirm our hypothesis that radio BHARs provide more stable lower limit estimates of the BHARs of any given AGN source. This could be achieved through similar studies using X-ray and radio selected AGN samples in the COSMOS field.

In future, decomposing the radio emission from SC4K sources using the IRRC may be useful in helping to isolate the radio emission component due to AGN activity from that caused by star formation. Hence, more accurate radio BHARs could be calculated, without risk of over-estimation due to contamination. This would be especially useful for the disky galaxies within our sample, which we believe host less active AGN.

Further study of the morphologies of the AGN host galaxies would also help to better characterise their evolution across cosmic time. Classifying these galaxies in multiple different wavebands may help to reduce the effect of the central SMBH outshining the entire galaxy and lead to fewer point-like or compact classifications, though we acknowledge that highly luminous AGN such as we have here tend to be exceptionally bright in almost all wavelengths.

including NumPy & SciPy (Van Der Walt et al. 2011; Jones et al. 2001), Matplotlib (Hunter 2007), Astropy (Astropy Collaboration et al. 2013) and the Topcat analysis program (Taylor 2013). This research has made use of the VizieR catalogue access tool, CDS, Strasbourg, France and the COSMOS Cutouts service provided by the NASA/IPAC IR Science Archive.

REFERENCES

Aird J., et al., 2010, MNRAS, 401, 2531
Angione R. J., 1973, AJ, 78, 353
Arnaud M., Rothenflug R., Boulade O., Vigroux L., Vangioni-Flam E., 1992, A&A, 254, 49
Astropy Collaboration et al., 2013, A&A, 558, A33
Barlow-Hall C., Bramwell J., Hodder D., Merrett M., Russ A., Wareing O., Sobral D., 2019, Notices of Lancaster Astrophysics (NLUAstro), 1, 39
Barth A. J., Martini P., Nelson C. H., Ho L. C., 2003, ApJ, 594, L95
Begelman M. C., Volonteri M., Rees M. J., 2006, MNRAS, 370, 289
Bondi M., Ciliegi P., Schinnerer E., Smolčić V., Jahnke K., Carilli C., Zamorani G., 2008, ApJ, 681, 1129
Brandt W. N., Alexander D. M., 2010, Proceedings of the National Academy of Science, 107, 7184
Calhau J., Sobral D., Stroe A., Best P., Smail I., Lehmer B., Harrison C., Thomson A., 2017, MNRAS, 464, 303
Calhau J., et al., 2020, MNRAS, 493, 3341
Charlot S., Fall S. M., 1993, ApJ, 415, 580
Chen H., 2019, arXiv e-prints, p. arXiv:1911.09113
Civano F., et al., 2016, ApJ, 819, 62
Cristiani S., et al., 2004, ApJ, 600, L119
Davies M. B., Miller M. C., Bellovary J. M., 2011, ApJ, 740, L42
Delhaize J., et al., 2017, A&A, 602, A4
Delvecchio I., et al., 2014, MNRAS, 439, 2736
Delvecchio I., et al., 2018, MNRAS, 481, 4971
Devecchi B., Volonteri M., 2009, ApJ, 694, 302
Dunn J. P., et al., 2010, ApJ, 709, 611
Elmer E., Almaini O., Merrifield M., Hartley W. G., Maltby D. T., Lawrence A., Botti I., Hirst P., 2020, MNRAS,
Elvis M., et al., 2009, ApJS, 184, 158
Fabian A. C., 2012, ARA&A, 50, 455
Fabian A. C., Iwasawa K., 1999, MNRAS, 303, L34
Ferrarese L., Ford H., 2005, Space Sci. Rev., 116, 523
Green R. F., 2002, AGN and the Demographics of Supermassive Black Holes. p. 335
Gürkan M. A., Fregeau J. M., Rasio F. A., 2006, ApJ, 640, L39
Hashimoto T., et al., 2017, A&A, 608, A10
Hathi N. P., Le Fèvre O., 2016, in Kaviraj S., ed., IAU Symposium Vol. 319, Galaxies at High Redshift and Their Evolution Over Cosmic Time. pp 22–25 (arXiv:1603.05992), doi:10.1017/S174392131501039X
Hawkins M. R. S., 2007, A&A, 462, 581
Hirschmann M., Somerville R. S., Naab T., Burkert A., 2012, MNRAS, 426, 237
Hunter J. D., 2007, Computing In Science & Engineering, 9, 90
Jones E., Oliphant T., Peterson P., et al., 2001, SciPy: Open source scientific tools for Python, http://www.scipy.org/
Koekemoer A. M., et al., 2007, ApJS, 172, 196
Körding E. G., Fender R. P., Migliari S., 2006, MNRAS, 369, 1451
Körding E. G., Jester S., Fender R., 2008, MNRAS, 383, 277
Kormendy J., Richstone D., 1995, ARA&A, 33, 581
Kubota A., Makishima K., Ebisawa K., 2001, ApJ, 560, L147
Laursen P., Duval F., Östlin G., 2013, ApJ, 766, 124
Lehmer B. D., et al., 2013, ApJ, 765, 87

Lehmer B. D., et al., 2016, ApJ, 825, 7
Lodato G., Natarajan P., 2006, MNRAS, 371, 1813
Madau P., Rees M. J., 2001, ApJ, 551, L27
Malhotra S., Rhoads J. E., 2002, ApJ, 565, L71
Marchesi S., et al., 2016, ApJ, 827, 150
Marconi A., Risaliti G., Gilli R., Hunt L. K., Maiolino R., Salvati M., 2004, MNRAS, 351, 169
Markevitch M., et al., 2003, ApJ, 583, 70
Marshall N., Warwick R. S., Pounds K. A., 1981, MNRAS, 194, 987
Matute I., La Franca F., Pozzi F., Gruppioni C., Lari C., Zamorani G., 2006, A&A, 451, 443
McNamara B. R., Nulsen P. E. J., 2007, ARA&A, 45, 117
Merloni A., 2004, MNRAS, 353, 1035
Meurs E. J. A., Wilson A. S., 1984, A&A, 136, 206
Moe M., Arav N., Bautista M. A., Korista K. T., 2009, ApJ, 706, 525
Nandra K., 2009, in astro2010: The Astronomy and Astrophysics Decadal Survey. p. 220 (arXiv:0903.0547)
Netzer H., 2015, ARA&A, 53, 365
Neufeld D. A., 1991, ApJ, 370, L85
Neugebauer G., Soifer B. T., Matthews K., Elias J. H., 1989, AJ, 97, 957
Oke J. B., Gunn J. E., 1983, ApJ, 266, 713
Oteo I., Sobral D., Ivison R. J., Smail I., Best P. N., Cepa J., Pérez-García A. M., 2015, MNRAS, 452, 2018
Paulino-Afonso A., et al., 2018, MNRAS, 476, 5479
Pozdnyakov L. A., Sobol I. M., Syunyaev R. A., 1983, Astrophysics and Space Physics Reviews, 2, 189
Rafferty D. A., McNamara B. R., Nulsen P. E. J., Wise M. W., 2007, in Böhringer H., Pratt G. W., Finoguenov A., Schuecker P., eds, Heating versus Cooling in Galaxies and Clusters of Galaxies. p. 121 (arXiv:astro-ph/0612258), doi:10.1007/978-3-540-73484-0_23
Saez C., Chartas G., Brandt N., 2009, in American Astronomical Society Meeting Abstracts #213. p. 608.02
Sargsyan L. A., Weedman D. W., 2009, ApJ, 701, 1398
Shapiro S. L., Lightman A. P., Eardley D. M., 1976, ApJ, 204, 187
Smolčić V., et al., 2017, A&A, 602, A1
Sobral D., Santos S., Matthee J., Paulino-Afonso A., Ribeiro B., Calhau J., Khostovan A. A., 2018a, MNRAS, 476, 4725
Sobral D., et al., 2018b, MNRAS, 477, 2817
Soltan A., 1982, MNRAS, 200, 115
Somerville R. S., Davé R., 2015, ARA&A, 53, 51
Springel V., et al., 2005, Nature, 435, 629–636
Taylor M., 2013, Starlink User Note, 253
Van Der Walt S., Colbert S. C., Varoquaux G., 2011, Computing in Science & Engineering, 13, 22
Volonteri M., 2010, A&ARv, 18, 279
Volonteri M., Haardt F., Madau P., 2003, ApJ, 582, 559
White S. D. M., Rees M. J., 1978, MNRAS, 183, 341
Willott C. J., Percival W. J., McLure R. J., Crampton D., Hutchings J. B., Jarvis M. J., Sawicki M., Simard L., 2005, ApJ, 626, 657
Wisotzki L., et al., 2016, A&A, 587, A98
Wolf C., Wisotzki L., Borch A., Dye S., Kleinheinrich M., Meisenheimer K., 2003, A&A, 408, 499

This paper has been typeset from a TeX/LaTeX file prepared by the author.